Mass and Energy Budgets of a 1 km High Atmospheric Box over the GATE C-Scale Triangle during Undisturbed and Disturbed Weather Conditions

BURGHARD BRÜMMER

Sonderforschungsbereich 94, Universität Hamburg, Max-Planck-Institut für Meteorologie, Hamburg, West Germany

(Manuscript received 15 August 1977, in final form 18 January 1978)

ABSTRACT

Using vertical wind, temperature and humidity profiles in the C-scale triangle during GATE from 2–5 September 1974, the budgets of mass, latent heat and dry and moist static energy are calculated in the lowest kilometer of the atmosphere. The computations are performed for intervals of 3–6 h. Using radar pictures the results are classified as "undisturbed" or "disturbed" with respect to the convective activity.

The horizontal flow near the sea surface is nearly always convergent. During disturbed situations the low-level convergence ($\sim 10^{-4}$ s^{-1}) is about one order of magnitude larger than during undisturbed conditions. When relating the convection (radar echo covergage) to the low-level convergence it is found that a certain background value of convergence must be exceeded before radar echoes (raining convection) develop and that the convection reacts with a delay of 3–4 h to variations of the low-level divergence.

During disturbed situations the subgrid-scale flux of moist static energy at the sea surface is about 30% greater than during undisturbed conditions. The flux is constant with height in undisturbed conditions but increases with height in disturbed situations. At cloud base the subgrid-scale flux of moist static energy is about twice as large in disturbed conditions (180 W m^{-2}) as in undisturbed conditions (100 W m^{-2}).

1. Introduction

In recent years budget studies of mass, energy and momentum using data from ship arrays of about 500 km×500 km grid size in Atlantic trade wind regions have been successfully performed [e.g., with data from the Atlantic Trade Wind Experiment (ATEX) 1969 (Augstein *et al.*, 1973; Brümmer, 1976) and from the Barbados Oceanographic and Meteorological Experiment (BOMEX) 1969 (Holland and Rasmusson, 1973; Nitta and Esbensen, 1974; Esbensen, 1975)]. These studies have increased our understanding of atmospheric processes in the marine trade wind regions.

Among the main objectives of the 1974 GARP Atlantic Tropical Experiment (GATE) were the analysis of meteorological events of different scales in the regions of the intertropical convergence zone (ITCZ) and the investigation of the relations between the scales involved (Houghton, 1974). To achieve these goals, three stationary ship arrays covered the area of the ITCZ in the eastern part of the Atlantic ocean during the third phase of the experiment lasting from 30 August–17 September 1974 (Fig. 1). Three areas were involved: 1) the A/B-scale hexagon with mean diameter of about 700 km, 2) the B-scale hexagon with a mean diameter of about 300 km and 3) the C-scale triangle with a mean side length of about 100 km.

In this study the budget method is applied to an atmospheric box of about 1 km height over the smallest horizontal array, the C-scale triangle, during a 4-day period, 2–5 September 1974. The corner points of the triangle were formed by R.V. *Meteor* (8.52°N, 23.45°W), R.V. *Planet* (9.24°N, 22.99°W) and R.V. *Fay* (8.50°N, 22.58°W). The budgets of mass, latent heat and dry and moist static energy were calculated. The results are classified as "undisturbed" and "disturbed" with respect to the different levels of convective activity in the C-scale region. The budgets are compared with corresponding calculations for the larger ship arrays during GATE and for the oceanic trade wind regions as observed during ATEX and BOMEX.

Section 2 deals with the weather situation and the mode classification scheme, Section 3 with the data used and Section 4 with the computational procedure. In Section 5 the different thermodynamical structure during undisturbed and disturbed weather situations is discussed. Section 6 is concerned with the mass budget, the relationship between the low-level mass divergence and the convective activity. Section 7 deals with the energy budgets; and grid-scale and subgrid-scale vertical energy transports during undisturbed and disturbed weather conditions are discussed.

2. Weather situation and mode classification

Considerable variations of the weather conditions in the region of the C-scale triangle occurred during the period 2–5 September 1974, ranging from nearly cloud-

0022-4928/78/0997-1011$07.50

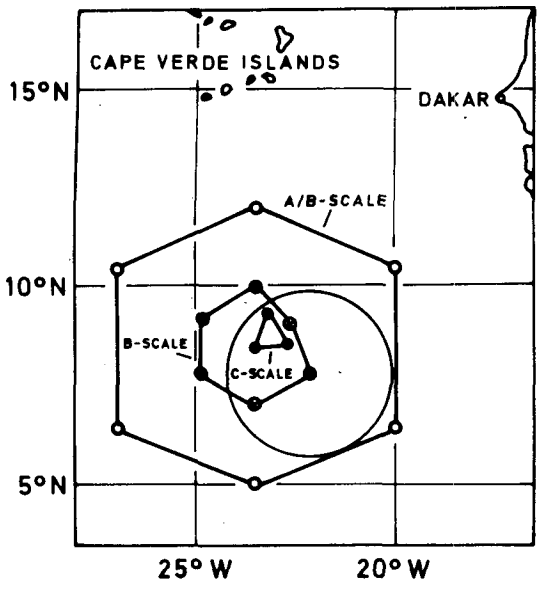

FIG. 1. Positions of ship arrays during the third phase of GATE: C-scale triangle and B-scale and A/B-scale hexagons. The circle marks the horizontal range of the *Oceanographer* radar instrument.

less skies or small amounts of low-level clouds within a radius of some hundred kilometers around the ships to large cumulonimbus systems inside the triangle. During these four days two easterly waves passed over the C-scale area according to an analysis by Thompson (1977). The trough of the first wave passed during the noon hours on 2 September, the second during the afternoon on 5 September. Compared to the "average GATE situation" the period 2–5 September seems to represent a typical sequence of large-scale weather situations. It may be assumed, therefore, that the results from this special period may be valid in a more general sense for the ITCZ region.

In order to perform separate budget calculations for different weather situations, hourly radar pictures from the R.V. *Oceanographer* (situated ~100 km southeast of the C-scale triangle; see Fig. 1) are used to select time intervals of nearly stationary weather conditions. In this way the 4-day period is subdivided into 14 intervals of about 3–6 h. Since there were some gaps in the data, the whole period could not be covered by these intervals. The weather situation for each interval is characterized by a representative radar picture in Fig. 2. The periods 1000–1400 GMT and 1400–1700 GMT on 2 September do not fit into our scheme due to rapid time changes of the large-scale field; for these cases two pictures are presented which show the extreme situations. The lack of data prevented further subdivision of these two intervals.

At this stage of the GATE analysis it may be reasonable to capitalize on the very obvious differences between undisturbed and disturbed conditions. Therefore, we distinguish only between cases of less than 5% radar echo area coverage in the C-scale triangle (undisturbed; insignificant rainfall) and those of more than 5% echo coverage (disturbed; significant rainfall). For all undisturbed and disturbed cases the percentage area coverage of radar echoes in the triangle and the tendency during the respective time interval are listed in Table 1. At a later stage of the GATE analysis, when budgets for the whole third phase of the experiment are available, it may be useful to distinguish between periods of increasing, steady and decreasing echo coverage or to classify with respect to the different parts of the easterly wave.

3. The data

During the period 2–5 September 1974, vertical wind profiles were measured every 45 min by means of radar systems on the *Meteor* and *Planet* and every hour by means of an optical theodolite on the *Fay*. The azimuth and elevation angles measured by the theodolite are completed by height estimates from pressuresondes which were attached to the tracked pibal. At times the wind profile could be obtained only up to cloud base due to the general restrictions of optical tracking. We presume that the individual radar and theodolite wind

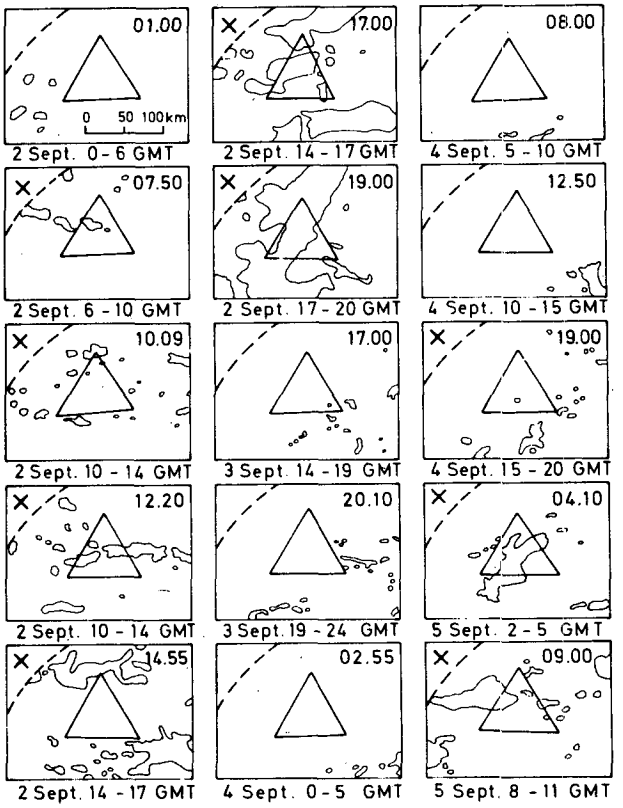

FIG. 2. Representative radar pictures from the *Oceanographer* in the region of the C-scale triangle for the individual time intervals. The time interval is indicated below each picture; the time the picture was taken is given in the right upper corner (all times GMT). Crosses in the left upper corner mark those time intervals which are classified as "disturbed."

profiles are accurate to within 1 m s^{-1} up to 1 km height. Difficulties with the *Meteor* and *Planet* radar systems caused some gaps in the 45 min series of the wind profiles obtained at these locations. Vertical profiles of the thermodynamic parameters (temperature, humidity and pressure) were measured by means of a special German radiosonde every 3 h from all three platforms; the absolute accuracies of these data are on the order of 0.1°C, 0.2 g kg^{-1} and 0.5 mb, respectively. In addition to these aerological measurements, surface observations of the standard meteorological parameters including water temperature, cloudiness and rainfall amount and duration were carried out at 1 h intervals.

The number of wind and structure profiles used at each ship for the budget calculations during the individual time intervals are listed in Table 2. The computations are based on three to nine wind profiles and one to two structure profiles at each station. The small number of structure profiles is not of great consequence, since the results of the budget calculations depend primarily on an accurate mass balance.

4. The computational procedure

Averaging the budget equations of mass, latent heat and dry and moist static energy over a time interval $\Delta\tau$ (temporal average denoted by an overbar) and over the area F of the C-scale triangle (areal average denoted by a tilde), and integrating vertically from the base z_b to the top z_t of a certain layer the following equations are obtained:

Mass

$$\underbrace{\int_{z_b}^{z_t}(1/\Delta\tau)(\tilde{\rho}_{\Delta\tau}-\tilde{\rho}_0)dz}_{R_1}+\underbrace{\int_{z_b}^{z_t}F^{-1}\oint\bar{\rho}\bar{v}_n dldz}_{R_2}+\underbrace{(\widetilde{\bar{\rho}\bar{w}})_t}_{R_3}-\underbrace{(\widetilde{\bar{\rho}\bar{w}})_b}_{R_4}=0 \quad (1)$$

Latent heat Lq

$$\underbrace{\int_{z_b}^{z_t}(L/\Delta\tau)(\widetilde{\rho q}_{\Delta\tau}-\widetilde{\rho q}_0)dz}_{Q_1}+\underbrace{\int_{z_b}^{z_t}F^{-1}\oint L\bar{\rho}\bar{q}\bar{v}_n dldz}_{Q_2}+\underbrace{(\widetilde{L\bar{\rho}\bar{q}\bar{w}})_t}_{Q_3}-\underbrace{(\widetilde{L\bar{\rho}\bar{q}\bar{w}})_b}_{Q_4}+\underbrace{(\widetilde{L\bar{\rho}\overline{q'w'}})_t}_{Q_5}-\underbrace{(\widetilde{L\bar{\rho}\overline{q'w'}})_b}_{Q_6}=-\underbrace{\int_{z_b}^{z_t}L\bar{\rho}(\widetilde{d\bar{q}/dt})_{c,e}dz}_{Q_7} \quad (2)$$

TABLE 1. Time intervals in undisturbed and disturbed weather situations with the corresponding radar echo area coverage in the C-scale triangle and its tendency.

Date	Time (GMT)	Percent area radar echoes	Tendency
	Undisturbed cases		
2 September	0000–0600	0	—
3 September	1400–1900	0–5	⌟
	1900–2400	2–5	—
4 September	0000–0500	0	—
	0500–1000	0	—
	1000–1500	0	—
	Disturbed cases		
2 September	0600–1000	10	⌐
	1000–1400	15	⌐
	1400–1700	1–50	/
	1700–2000	50	⌐
4 September	1500–2000	0–10	/
5 September	0200–0500	35	—
	0800–1100	25	—
	0000–1500	30	—

Dry static energy $s=c_pT+gz$

$$\underbrace{\int_{z_b}^{z_t}(1/\Delta\tau)(\widetilde{\rho s}_{\Delta\tau}-\widetilde{\rho s}_0)dz}_{S_1}+\underbrace{\int_{z_b}^{z_t}F^{-1}\oint\bar{\rho}\bar{s}\bar{v}_n dldz}_{S_2}+\underbrace{(\widetilde{\bar{\rho}\bar{s}\bar{w}})_t}_{S_3}-\underbrace{(\widetilde{\bar{\rho}\bar{s}\bar{w}})_b}_{S_4}+\underbrace{(\widetilde{\bar{\rho}\overline{s'w'}})_t}_{S_5}-\underbrace{(\widetilde{\bar{\rho}\overline{s'w'}})_b}_{S_6}=\underbrace{\int_{z_b}^{z_t}L\bar{\rho}(\widetilde{d\bar{q}/dt})_{c,e}dz}_{S_7}+\underbrace{\int_{z_b}^{z_t}c_p\bar{\rho}(\widetilde{d\bar{T}/dt})_{\mathrm{Rad}}dz}_{S_8} \quad (3)$$

TABLE 2. Number of wind (RW) and structure (SS) profiles at each ship used for the computations during the individual time intervals.

Date	Time (GMT)	*Meteor* RW	*Meteor* SS	*Planet* RW	*Planet* SS	*Fay* RW	*Fay* SS
	Undisturbed cases						
2 September	0000–0600	6	1	6	2	7	2
3 September	1400–1900	7	2	8	2	4	2
	1900–2400	6	2	7	1	3	2
4 September	0000–0500	6	1	8	2	7	2
	0500–1000	6	1	8	1	5	1
	1000–1500	3	1	9	2	5	2
	Disturbed cases						
2 September	0600–1000	5	1	8	1	4	1
	1000–1400	5	2	3	2	4	2
	1400–1700	3	1	1	1	1	1
	1700–2000	3	1	3	1	4	2
4 September	1500–2000	7	1	9	1	4	2
5 September	0200–0500	2	1	3	1	3	1
	0800–1100	3	1	6	1	3	1
	0000–1500	9	4	15	5	8	5

Moist static energy $h=c_pT+gz+Lq$

$$\underset{H_1}{\int_{z_b}^{z_t} 1/\Delta\tau(\widetilde{\rho h}_{\Delta\tau}-\widetilde{\rho h}_0)dz}+\underset{H_2}{\int_{z_b}^{z_t} F^{-1}\oint \bar{\rho}\bar{h}\bar{v}_n dl dz}$$

$$+\underset{H_3}{(\widetilde{\bar{\rho}\bar{h}\bar{w}})_t}-\underset{H_4}{(\widetilde{\bar{\rho}\bar{h}\bar{w}})_b}+\underset{H_5}{(\widetilde{\bar{\rho}\overline{h'w'}})_t}-\underset{H_6}{(\widetilde{\bar{\rho}\overline{h'w'}})_b}$$

$$=\underset{H_8}{\int_{z_b}^{z_t} c_p\bar{\rho}(\widetilde{d\bar{T}/dt})_{\mathrm{Rad}}dz}. \quad (4)$$

The symbols v_n, w, q, T, ρ and z represent the component of the horizontal wind vector normal to the legs of the triangle, vertical velocity, specific humidity, temperature, density and height, respectively; L, c_p and g represent the latent heat of condensation, the specific heat at constant pressure and the earth's gravity, respectively. The indices t and b denote values at the top and base of the layer and the indices 0 and $\Delta\tau$ mark values at the beginning and end of the time interval. The indices c, e and Rad refer to net condensation/evaporation and to radiation, respectively.

Each term in (1)–(4) is symbolized by a capital letter and an index number. The index 1 terms denote the local time change and the index 2 terms the divergence of the mean horizontal transports. The index 3 and 4 terms represent the grid-scale vertical transports at the top and base of the layer, respectively; the index 5 and 6 terms the respective subgrid-scale vertical transports. The index 7 and 8 terms denote the sources or sinks of energy due to condensation or evaporation of water and due to radiation, respectively.

Provided that the grid-scale vertical motion is zero at the surface, its vertical profile can be calculated from Eq. (1). Using these results, the grid-scale vertical energy transports at the top (Q_3, S_3, H_3) and the base (Q_4, S_4, H_4) of the layer are computed. Since the sink and source terms were not measured during GATE, they are estimated by means of model assumptions. The radiation term (S_8, H_8) is calculated by models of Rodgers and Walshaw (1966) for the longwave part of the spectrum and Korb *et al.* (1958) for the shortwave radiation. The effects of clouds are roughly incorporated into these models. The coverage with low-level and higher level clouds is taken from the hourly surface observations at the corner ships and at *Hecla* (8.8°N, 23.0°W) which was situated nearly in the center of the C-triangle. The heights and thicknesses of the clouds are estimated from the thermodynamic profiles. The computed radiational cooling or heating rates are in the range of the climatic data given by Dopplick (1972). The method of estimating the condensation/evaporation term (Q_7, S_7) will be described in detail in Section 7. The subgrid-scale vertical energy fluxes at the top of the layer (Q_5, S_5, H_5) are then computed as residual terms after their values at the sea surface have been determined by the bulk aerodynamic formulas

$$(L\bar{\rho}\overline{q'w'})_0=c_EL\rho V_{10}\Delta q_{10}, \quad (5)$$

$$(\bar{\rho}\overline{s'w'})_0=c_Hc_p\rho V_{10}\Delta\theta_{10}, \quad (6)$$

$$(\bar{\rho}\overline{h'w'})_0=(L\bar{\rho}\overline{q'w'})_0+(\bar{\rho}\overline{s'w'})_0, \quad (7)$$

where V_{10} is the wind speed at 10 m and Δq_{10}, $\Delta\theta_{10}$ are the differences of the specific humidity and potential temperature between the sea surface and 10 m. The transport coefficients c_E and c_H are assumed to be constant in time and space and are taken as 1.4×10^{-3} for c_E and 1.5×10^{-3} for c_H. The uncertainties of these coefficients are in the range of $\pm0.4\times10^{-3}$.

The integration with respect to height in Eqs. (1)–(4) is executed for 100 m thick layers step by step starting from the sea surface. In the derivation of (1)–(4) linearity of the wind vector, temperature and humidity between the three research vessels had to be assumed and the divergence of subgrid-scale horizontal transports as well as the storage of moisture and heat within clouds associated with an unstationary cloud population were neglected. These simplifications clearly contribute to the uncertainties of our results. An estimate of the magnitude of these uncertainties is given in Section 7, where the results with respect to the residual terms (Q_5, S_5, H_5) are discussed.

5. The thermodynamic structure in undisturbed and disturbed weather zones

Using the 3 h temperature and humidity profiles, the thermodynamic structure in the lowest 2 km of the atmosphere during undisturbed and disturbed weather conditions is analyzed. As can be seen from Fig. 2, radar echoes (rain) never occur over the whole C-scale triangle simultaneously, not even during strongly disturbed conditions. Consequently, in a disturbed situation the location at which the thermodynamic profile is observed can have a considerable effect. Therefore, to account for the local nature of the measurement the investigation of the structure is performed for each ship separately. A profile is regarded as representing the undisturbed state of the atmosphere when there are no radar echoes within a radius of at least 10 n mi around the platform and no rain was observed in the preceding 2 h. Profiles measured during rain periods or not later than 1 h after a rain period are termed disturbed.

This classification is applied to all profiles during the third phase of the GATE. Since the results for the three ships do not differ significantly, the mean temperature and humidity profiles for undisturbed and disturbed situations are given in Fig. 3. The curves representing the undisturbed state of the atmosphere are based on 53 *Meteor*, 72 *Planet* and 80 *Fay* profiles; those repre-

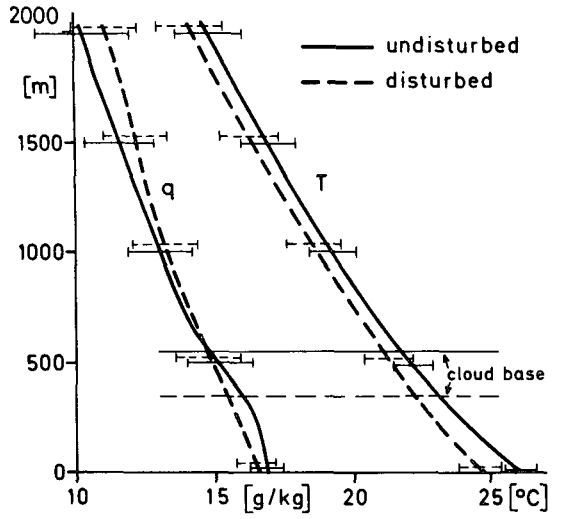

FIG. 3. Mean profiles of temperature (T) and specific humidity (q) during undisturbed (solid) and disturbed (dashed) weather situations. The profiles represent averages over the ships *Meteor*, *Planet* and *Fay* and over the whole third phase of GATE (30 August–17 September). Horizontal bars represent the standard deviation. The cloud base levels are indicated by the long horizontal lines.

senting the disturbed state are based on 33 *Meteor*, 33 *Planet* and 37 *Fay* profiles.

In disturbed weather zones the temperature is about 0.5–1.5°C lower than in the undisturbed surroundings. The main cooling occurs in the subcloud layer. In the disturbed state, lower values of moisture are observed in the subcloud layer and larger values in the upper part of the cloud layer as compared to the undisturbed state. Only insignificant humidity variations occur in the lower part of the cloud layer. These marked differences between the undisturbed and disturbed state of the atmosphere can be attributed to the effects of rain and vertical motions. Rain which falls from above into the layer partly evaporates and leads to a decrease in the actual temperature and an increase in the moisture content. If the evaporation is constant with height this would only shift the temperature and moisture profile. The rain effect is additionally modified by intensive updrafts and downdrafts associated with large clouds which generally transport warm and moist air upward and cool and dry air downward. Therefore relatively cooler and drier air comes into the subcloud layer and relatively warmer and moister air into the cloud layer. The small moisture differences in the lower part of the cloud layer may indicate that the updrafts generally penetrate these levels without any considerable detrainment.

Due to the averaging at constant levels applied in Fig. 3, details of the structure are lost. However, the individual profiles in undisturbed regions show a stratification similar to the undisturbed trades with a mixed layer, a transition layer and a conditionally unstable stratified cloud layer (Augstein *et al.*, 1974). A permanent temperature inversion at a nearly constant level, such as the trade wind inversion, is not observed in the undisturbed ITCZ region. However, after the passage of strong disturbances, transient temperature inversions at several levels are often observed. Generally they exist no longer than a few hours. Sometimes the lowest inversion is clearly below the lifting condensation level and then it represents the top of the mixed layer; in those cases any convection from below through that level is suppressed. These transient structure features seem to be associated with compensatory downward motions on a scale of a few kilometers to about ten kilometers after the passage of a disturbance.

6. Mass budget

The computed divergence of the grid-scale horizontal flow in the lowest 1000–1500 m of the atmosphere for the individual undisturbed and disturbed time intervals is shown in Fig. 4. The average values for all un-

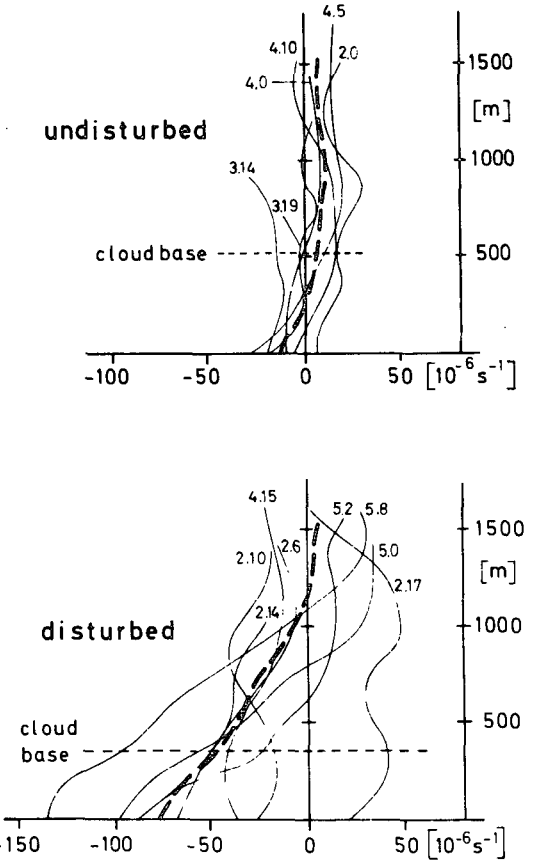

FIG. 4. Vertical profiles of the divergence of the horizontal flow in the C-scale triangle during the individual undisturbed and disturbed time intervals. The numbers at each curve mark the day of September and the beginning of the respective interval from Table 1 (for example, 3.14 means the time interval on 3 September from 1400–1900 GMT). The average of the undisturbed and the disturbed cases is indicated by a heavy dashed line. The time interval on 2 September from 1700–2000 GMT is omitted in the average of the disturbed cases.

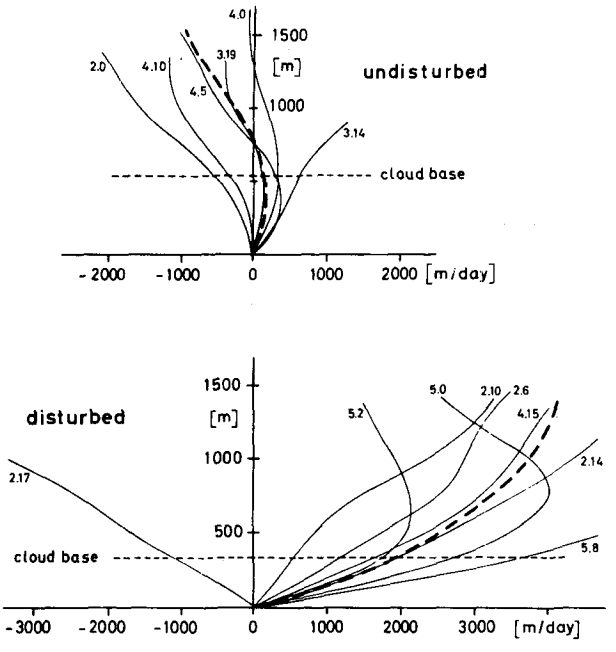

FIG. 5. Vertical profiles of the grid-scale vertical motion in the C-scale triangle during the individual undisturbed and disturbed time intervals. Otherwise see legend to Fig. 4.

disturbed and disturbed cases are indicated by heavy dashed lines. Assuming an error of about 1 m s^{-1} for the individual wind measurement and using three to nine wind profiles at each corner of the triangle for one period, the inaccuracy of the divergence profiles for the individual time intervals is on the order of 10^{-6} s^{-1}. The uncertainty may increase slightly with height since the data coverage decreases particularly above cloud base.

The computations show that undisturbed weather situations are characterized by a weak convergence near the sea surface and by a divergence of similar magnitude in the cloud layer. The low-level convergent flow is confined to a layer only a few hundred meters thick. During disturbed situations the convergence values near the surface are about one order of magnitude larger than during undisturbed conditions. The flow stays convergent up to the lower part of the cloud layer. The differences between undisturbed and disturbed situations indicate that a certain background value of the low-level divergence on the order of 10^{-5} s^{-1} has to be exceeded until radar echoes (raining convection) develop. The convergence profile for the period 1700–2000 GMT on 2 September 1974 departs totally from the others of the disturbed category. In spite of the large radar echo coverage of about 50% a divergent flow is derived in the lowest 1000 m of the atmosphere. From other observations it can be inferred that the convective system is in its decaying stage: only a slight drizzle is measured on *Meteor* and *Planet*, temperature profiles at all three ships at 1930 GMT show several inversions in the lowest 2 km, and at 2200 GMT all radar echoes have disappeared over the triangle. The observations for this period indicate a certain time lag between the grid-scale divergence of the low-level wind field and the convective activity estimated from the radar echo coverage. This point will be considered in more detail later in this section.

The vertical motions calculated from the divergence profiles are displayed in Fig. 5. During undisturbed conditions on the average an upward grid-scale motion is derived in the mixed layer and a downward motion in the cloud layer. The upward motion in the subcloud layer seems to be overruled by the subsidence in the cloud layer which prevents cloud growth into high altitudes. Cloud tops during undisturbed conditions are mainly below 2 km as can be seen from the temperature and humidity profiles passing through clouds and also from the observations of Borikov *et al.* (1975). At cloud base the grid-scale vertical velocity is small but, on the average, positive. Since in the cloud-free areas a stable transition layer between the mixed layer and the cloud layer is always observed, suggesting that a downward motion is present there, the nonraining low-level clouds consequently transport more mass upward than is horizontally supplied by the large-scale convergent flow. Such a relationship was already found by Yanai *et al.* (1973).

During disturbed weather situations large upward velocities in the subcloud layer as well as in the lower part of the cloud layer are found, thus favoring cumulus convection. The grid-scale vertical motion at the cloud-base level is about 100 m h^{-1}. These values are still considerably smaller than the upward velocities in active clouds. It seems probable that a qualitatively similar relationship between cloud mass transport and grid-scale mass transport at cloud base is valid as it is during undisturbed situations. However, this cannot be proven with our data. There are some indications of downward motions outside of the active regions of a disturbance from the observations of transient temperature inversions. However, nothing is known about the horizontal areas over which these phenomena take place.

In Fig. 6 the average divergence profiles for the C-scale triangle are compared with those representing the GATE A/B-hexagon and the trade wind regions (ATEX, BOMEX). The values of Petrosiants *et al.* (1975) for the A/B-array at the surface and the 850 mb level are averages for the whole first phase of GATE, lasting from 28 June–17 July 1974. Similar results for the third phase are not yet available. The undisturbed values of the A/B-hexagon are quite similar to those of the C-scale triangle. However, there are some marked differences between the results of the disturbed periods, when the convergence in the C-scale triangle is about eight times larger than in the A/B-hexagon near the surface. The differences between a weakly and strongly developed ITCZ are much more distinct in the smaller C-scale than they are in the 80 times larger A/B-array. For situations with a strongly developed ITCZ the

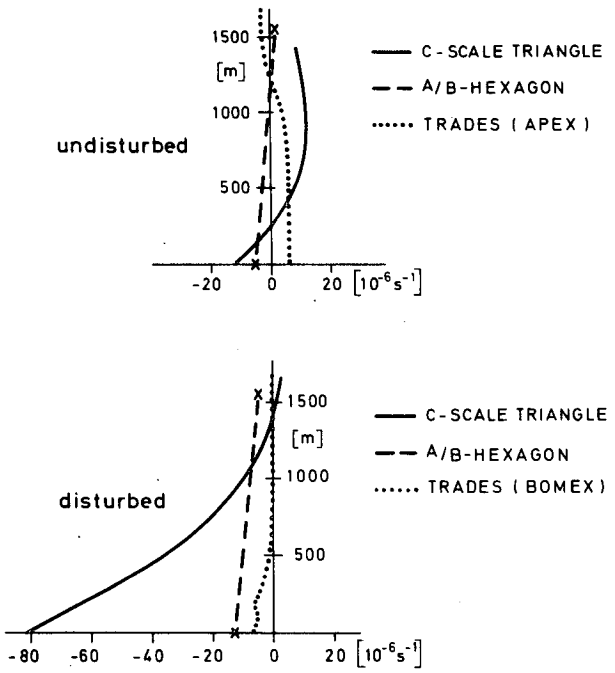

FIG. 6. Vertical profiles of the divergence of the large-scale horizontal flow in undisturbed and disturbed weather situations in the C-scale triangle (solid), in the A/B-hexagon (dashed) during GATE (Petrosiants *et al.*, 1975), and in the trades (dotted) during ATEX (Brümmer, 1976) and BOMEX (Esbensen, 1975).

convergence seems to be concentrated on a smaller horizontal scale. The undisturbed trade winds with divergent horizontal flow in the lowest 1000 m (Brümmer, 1976; Holland and Rasmusson, 1973) present even more unfavorable conditions for the development of deep cumulus convection than the undisturbed GATE regions. The mass divergence in disturbed trade wind areas (Esbensen, 1975) is rather similar to the undisturbed ITCZ case.

Fig. 4 indicates a distinct relationship between the echo area coverage and the convergence of the low-level flow. Since the variations of divergence are strongest near the sea surface, hourly values of the divergence calculated from the simultaneous surface wind observations at the three C-scale ships were correlated with the hourly radar observations from the *Oceanographer*. In the upper part of Fig. 7 the time series of the low-level divergence and the radar echo coverage in the C-scale triangle for an 8-day period from 1–8 September are displayed. A rough coherence between both curves is to be seen, at least for the long-period variations. From the cross-correlation function of both time series in the lower part of Fig. 7 it becomes evident that the best correlation is obtained for a time shift of 3–4 h, i.e., that the instantaneous convection (if the radar echo coverage can be taken as a measure of deep convective activity) is best correlated with the low-level divergence observed 3–4 h earlier. Thus the convective activity reacts with a certain time delay on variations of the large-scale low-level divergence. This time difference also contains the time delay between cloud formation (without echoes) and echo formation, which should be on the order of 1 h. Thus a distinct time difference between the large-scale forcing and the convection is still present, which may be considered as the adjustment introduced for this process by Arakawa and Schubert (1974). These authors have estimated that the time required to achieve equilibrium between both scales of motion is in the range 0.3–3 h.

In principle, a perfect correlation between the low-level divergence and the convection at a certain time delay cannot be expected because 1) the convection is additionally influenced by other processes such as the energy input from the sea surface, the divergence of the large-scale flow in the cloud layer or the stratification over a deep layer (Arakawa and Schubert, 1974); and 2) the adjustment time is not a constant value but should be dependent, for example, on the amplitude of the variation of the low-level large-scale forcing. Furthermore, the above derived time delay contains both directions of adjustment, i.e., the adjustment of growing convective systems to an increased large-scale forcing as well as the adjustment of decaying systems to a decreased forcing. It is not known whether for the decaying phase of a convective system the same adjustment time holds as for the growing phase. When more detailed radar data from the GATE area are available the adjustment may be investigated separately for the growing and decaying stage. Furthermore, it would be interesting to investigate the relationship between the

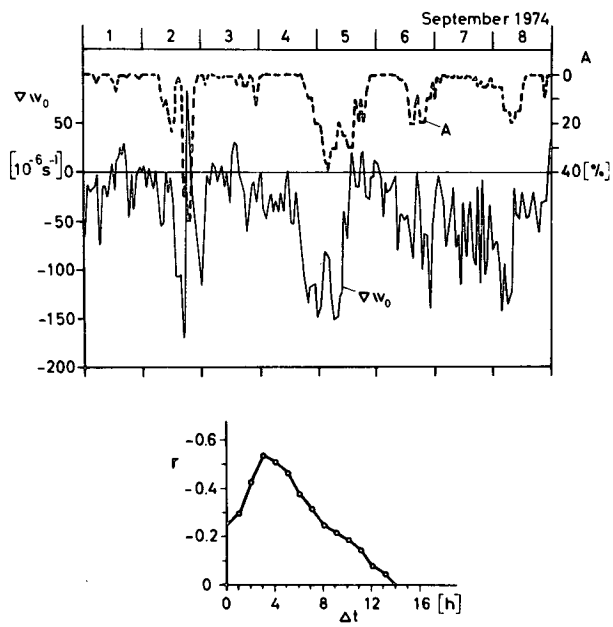

FIG. 7. *Above:* Time series of the divergence of the horizontal flow near the sea surface ($\nabla \cdot \mathbf{v}_0$, solid) and the radar echo area coverage (A, dashed) in the C-scale triangle during the period 1–8 September 1974. *Below:* Cross correlation (r) between both time series for different time shifts (Δt) of the divergence curve.

low-level mass divergence and the convective activity, also on larger scales.

7. The energy budgets

In this section the budgets of latent heat, dry static and moist static energy are discussed. Before dealing with the results, the method of estimating the net condensation/evaporation rate which appears in Eqs. (2) and (3) is presented. Since this term was not measured during GATE and cannot easily be measured in general, simple model assumptions had to be applied. For these estimates only those clouds or parts of clouds which are below the top of our calculation box are considered; these are mainly the low-level cumulus clouds. During disturbed situations, however, raining clouds can extend up to above 10 km (Shupiatsky *et al.*, 1975) and clouds are often observed with their bases far above the 1 km height of our calculation box (Simpson and Simpson, 1975). The evaporation of rain falling from these clouds into the box is neglected. The uncertainty introduced by this assumption with respect to the residual subgrid-scale flux is discussed in Section 7a. In order to estimate the net condensation/evaporation rate we make the following additional assumptions:

1) About 10% of the area (α) covered by an amount (n) of low-level clouds are updraft areas. This assumption represents an upper limit as can be concluded from tethered sonde measurements of the vertical motion in visible cloud areas (Emmitt, 1978). The amount of low-level clouds in the C-scale triangle is estimated from the hourly cloud observations at the three corner ships and at *Hecla* in the center.

2) The upward motion (w_{up}) in the updraft areas of the low-level clouds is 1 m s^{-1}.

3) The condensation rate can be derived on the basis of moist adiabatic changes of state of the ascending air in clouds.

Thus, we obtain the condensation rate

$$\left(\frac{dq}{dt}\right)_c = \alpha n w_{up} \frac{\Delta q_s}{\Delta z}, \tag{8}$$

where $\Delta q_s/\Delta z$ is the decrease of the saturation specific humidity q_s with height along a moist adiabate. In order to estimate the vertical distribution of the net condensation/evaporation rate it is further assumed:

4) During the undisturbed periods, mainly non-raining low-level clouds prevailed extending on the average from 500 m up to 1300 m; therefore, condensation and evaporation must cancel each other within the entire layer. It is further assumed that in the lower quarter of the clouds net condensation predominates and can be computed from Eq. (8), that condensation and evaporation locally balance each other in the second quarter of the cloud, and that evaporation predominates in the upper half of the clouds. This derived vertical distribution of the net condensation/evaporation rate is shown in Fig. 8; it is similar to that obtained from numerical model simulations of trade wind cumulus clouds by Sommeria (1976).

In disturbed situations most of the clouds extend up to several kilometers. Therefore, it is assumed that in the portion of the cloud layer with which we are concerned net condensation predominates, that it can be estimated from Eq. (8), and that it is constant with height (see Fig. 8). This last assumption may be too extreme since most of the low-level clouds which are also present in disturbed situations probably detrain and evaporate below the top of the calculation box.

These estimates are very coarse. For the interpretation of the residual subgrid-scale fluxes of latent heat and dry static energy this should be taken into account. However, the differences between the fluxes during undisturbed and disturbed situations should be qualitatively correct.

a. Budget of latent heat

In Fig. 8 the subgrid-scale vertical flux of latent heat during undisturbed and disturbed weather conditions is shown. The profiles represent average values of the respective class (see Table 1); the interval 1700–2000 GMT on 2 September is omitted in the average because it totally deviates from the other disturbed cases. The different curves indicate the fluxes if condensation/evaporation is neglected (solid) or if it is taken into account (dashed); the assumed net condensation or evaporation rates are shown by the diagrams to the right. The vertical profiles of the latent heat averaged over the individual time intervals and over the C-scale triangle are also given in Fig. 8.

During undisturbed weather conditions the subgrid-scale flux of latent heat is nearly constant or decreases slightly with height in the lowest 1000 m of the atmosphere. Consequently, the latent heat flux at cloud base is nearly as large as the local evaporation at the surface. However, for disturbed situations a quite different picture is obtained. Since disturbed conditions generally have drier air and stronger wind speeds near the sea surface, evaporation values about 30% larger than during undisturbed conditions are calculated from Eq. (5). Above the sea surface the latent heat flux increases with height in the lowest 1000 m. At cloud base about one-third more latent heat is transported upward by subgrid-scale processes than is locally supplied by evaporation from the sea surface. The moisture additionally needed must be advected by the convergent large-scale horizontal motion. An increase of the subgrid-scale latent heat flux with height during disturbed situations as opposed to the slightly decreasing or constant flux with height during undisturbed conditions is also derived from tethered balloon measurements in the subcloud layer during GATE (Thompson *et al.*, 1978). From investigations of the

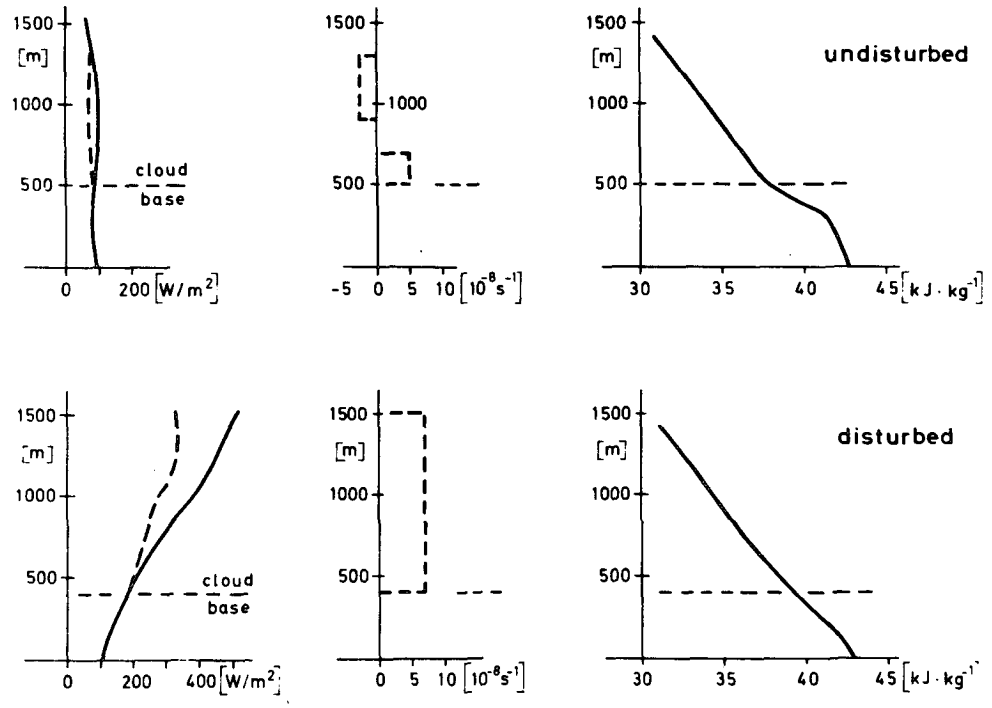

FIG. 8. *Left:* Average vertical profiles of the subgrid-scale vertical flux of latent heat in the C-scale triangle during undisturbed and disturbed weather situations without (solid) and with (dashed) consideration of net condensation or evaporation. *Middle:* Assumed vertical profiles of net condensation or evaporation during undisturbed and disturbed weather conditions. *Right:* Average vertical profiles of latent heat in the C-scale triangle during undisturbed and disturbed weather situations.

latent heat transports in clouds (Emmitt, 1978) it can be concluded that this increase can mainly be ascribed to the effects of intensive warm, moist updrafts and cold, dry downdrafts associated with deeper and larger clouds.

The individual contributions to the residual divergence of the subgrid-scale vertical latent heat flux $[Q_5+Q_6$ in Eq. (2)] are listed in Table 3. During undisturbed conditions, when the flux divergence is small, all contributions, such as the local time variation (Q_1) and the divergence of the three-dimensional grid-scale transport ($Q_2+Q_3+Q_4$) are also small. In the lower part of the cloud layer the net condensation (Q_7) is the dominating term. In disturbed situations the divergence of the grid-scale transports is the main contribution to the residual term at all levels; it is twice as large as the net condensation in the cloud layer.

The subgrid-scale and grid-scale vertical transports of latent heat are shown in Fig. 9. In undisturbed situations both transports are directed upward in the sub-cloud layer and have the same order of magnitude. Above cloud base the grid-scale transport is downward and becomes predominant. During disturbed weather conditions both fluxes are upward within the entire layer but the grid-scale transport is one order of magnitude larger.

In the next paragraphs we give some estimates of the uncertainties of the residual flux due to neglected terms in the budget equation (2) (e.g., storage of moisture in clouds, divergence of subgrid-scale horizontal flux, reevaporation of rain) and due to possible errors in the measurements (e.g., wind errors). If the areal average of the specific humidity in the cloud layer can be represented by

$$\bar{q}=q_{\mathrm{env}}(1-n)+nq_{cl}, \tag{9}$$

where n is the area covered by low-level clouds and q_{cl} and q_{env} are the specific humidity inside and around the clouds, respectively, then the local time derivative is given by

$$\frac{\partial\bar{q}}{\partial t}=\frac{\partial q_{\mathrm{env}}}{\partial t}+(q_{cl}-q_{\mathrm{env}})\frac{\partial n}{\partial t}+n\frac{\partial}{\partial t}(q_{cl}-q_{\mathrm{env}}). \tag{10}$$

Since the thermodynamic profiles at the three corner ships are mainly representative of the cloud environment, the first term on the right-hand side of (10) is given by the values of Q_1 in Table 3. The storage of latent heat in clouds is primarily represented by the second term of (10), because the third term is probably small compared to the second. In order to estimate the magnitude of the second term it is assumed that the air in the clouds is saturated at the temperature of the environment, i.e., $q_{cl}\approx q_s(T_{\mathrm{env}})$, and that the coverage with low-level clouds in the C-scale triangle is adequately represented by the cloud observations at the

Fig. 9), then the error in Q_5+Q_6 amounts to about ∓ 0.5 W m^{-2} for a 100 m thick layer near the surface and to about ∓ 7 W m^{-2} for a 100 m thick layer at

and of net condensation) ... diagrams to the right. The dry static energy per unit mass of air is also displayed in Fig. 10.

TABLE 3. Values for the individual terms in the budget equation (2) for latent heat for 100 m thick layers during undisturbed and disturbed situations. Q_1 represents the local time change, Q_2 the divergence of the mean horizontal transport, Q_3+Q_4 the divergence of the grid-scale vertical transport, Q_7 the latent heat source due to condensation or evaporation, and Q_5+Q_6 the residual divergence of the subgrid-scale vertical flux. All terms are in W m^{-2}.

Layer	Q_1	Q_2	Q_3+Q_4	$Q_2+Q_3+Q_4$	Q_7	Q_5+Q_6

out when integration along the legs. In order to obtain an estimate of the magnitude of the neglected term the following analysis is made. We assume that a mesoscale system extends over a 50 km long section of one leg of the triangle and that deviations of $|\mathbf{v}_n^*| \approx 1$ m s^{-1} and $q^* \approx 1$ g kg^{-1} are associated with it. Then, one would obtain a value of 2.5 W m^{-2} for Eq. (11) when inte-

TABLE 4. Values for the individual terms in the budget equation (3) for dry static energy for 100 m thick layers during undisturbed and disturbed situations. S_1 represents the local time change, S_2 the divergence of the mean horizontal transport, S_3+S_4 the divergence of the grid-scale vertical transport, S_7 and S_8 the dry static energy source due to condensation or evaporation and due to radiation, respectively, and S_5+S_6 the divergence of the subgrid-scale vertical flux. All terms are in W m^{-2}.

Layer	S_1	S_2	S_3+S_4	$S_2+S_3+S_4$	S_7	S_8	S_5+S_6
				Undisturbed			
0–100	−1.0	−355.7	+356.5	+0.8	0.0	−0.7	−0.5
100–200	−1.0	−183.3	183.3	0.0	0.0	−0.7	0.3
200–300	−1.0	−32.3	31.8	−0.5	0.0	−0.7	0.8
300–400	−1.0	68.3	−68.0	0.3	0.0	−0.7	0.0
400–500	−1.2	116.8	−117.3	−0.5	0.0	−0.7	1.0
500–600	−1.0	143.5	−144.5	−1.0	13.5	−1.0	14.5
600–700	−0.6	218.8	−220.0	−1.2	13.5	−1.0	14.3
700–800	−0.6	287.7	−287.2	0.5	0.0	−1.0	−0.4
800–900	−0.8	255.0	−255.2	−0.2	0.0	−1.0	0.0
900–1000	−0.7	260.0	−260.1	−0.1	−6.8	−1.0	−7.0
				Disturbed			
0–100	0.3	−2567.1	2568.7	1.6	0.0	0.0	−1.9
100–200	0.1	−2321.3	2324.7	3.4	0.0	0.0	−3.5
200–300	0.1	−1965.7	1973.0	7.3	0.0	0.0	−7.4
300–400	−0.1	−1609.7	1616.4	6.7	0.0	0.0	−6.6
400–500	−0.2	−1371.9	1381.6	9.7	18.9	−0.3	9.1
500–600	−0.1	−1170.9	1184.9	14.0	18.9	−0.3	4.7
600–700	0.3	−981.7	991.0	9.3	18.9	−0.3	9.0
700–800	0.2	−764.1	782.1	18.0	18.9	−0.3	0.4
800–900	0.0	−529.9	547.6	17.7	18.9	−0.3	0.9
900–1000	0.0	−294.9	311.1	16.2	18.9	−0.3	2.4

disturbed as in undisturbed areas. From tethered balloon measurements below and inside of larger clouds during GATE, Emmitt (1978) obtained a qualitatively similar profile of the sensible heat flux, with small values in the subcloud layer and an increase in the cloud layer. The flux profiles in Fig. 10 are also qualitatively similar to those derived for the undisturbed trade during ATEX (Brümmer, 1976).

The individual contributions to the residual term [S_5+S_6 in (3)] are listed in Table 4. In the undisturbed case all contributions, such as the local time variation (S_1), the divergence of the three-dimensional grid-scale transport ($S_2+S_3+S_4$), the radiational cooling (S_8) and the net condensation (S_7), are small and have the same order of magnitude. Only in the lower and upper part of the cloud layer is S_7 the dominating term. The magnitudes of the terms S_1 and S_8 are similar in the undisturbed and disturbed cases, but the sum of the terms $S_2+S_3+S_4$ is about one order of magnitude larger in the disturbed case. This term and the net condensation (S_7) represent the dominating contributions to the residual term in disturbed situations.

Calculating the divergence of the subgrid-scale flux of dry static energy as a residual term represents an

about 0.4 kJ kg^{-1} in the cloud layer (see Fig. 10), then the error in S_5+S_6 amounts to about ± 0.1 W m^{-2} for a 100 m thick layer near the surface and to about ± 4 W m^{-2} for a 100 m thick layer at 1000 m height. An overestimate of the divergence results in an overestimate of the residual term (S_5+S_6) and vice versa. These error values for S_5+S_6 are about half as large as the corresponding values for Q_5+Q_6 (see Section 7a) and have opposite signs due to the different vertical gradients $\partial s/\partial z$ and $\partial(Lq)/\partial z$ (see Figs. 8 and 10).

The storage of dry static energy in clouds, i.e., the term

$$\int_{z_b}^{z_t} (s_{cl}-s_{env})\frac{\partial n}{\partial t}dz, \tag{12}$$

has been neglected in the budget equation (3). In (12) s_{cl} and s_{env} represent the dry static energy inside and around the clouds. Neglecting (12) is probably not too restrictive because the temperature differences between the clouds and their environment are generally small and can have different signs. If for all parts of the visible cloud the temperature were 0.5°C warmer than the environment, the storage term would amount to about 0.5 W m^{-2} for a 100 m thick layer during the disturbed situation.

For the neglected divergence of the subgrid-scale horizontal flux of dry static energy, i.e., for the term

$$\int_{z_b}^{z_t} F^{-1}\oint \rho \mathbf{v}_n^* s^* dl dz, \tag{13}$$

where $\mathbf{v}_n^*$ and s^* represent deviations of $\mathbf{v}_n$ and s from the assumed linear relationship along the legs of the triangle, one obtains a value of 1.0 W m^{-2} for a 100 m thick layer, if there were a deviation of 1°C and 1 m s^{-1} along a 50 km long section of one leg of the triangle.

The grid-scale vertical transports of dry static energy and latent heat are compared in Fig. 11. The shapes of both profiles are similar, because they are mainly determined by the profile of the grid-scale vertical motion (Fig. 5). Since the dry static energy per unit mass of air is about ten times larger than the latent heat content, the grid-scale vertical transports of both quantities also differ by a factor of 10. The grid-scale transport of dry static energy is about two powers of ten larger than the subgrid-scale flux during undisturbed conditions and about three powers of 10 larger during disturbed situations.

c. *Budget of moist static energy*

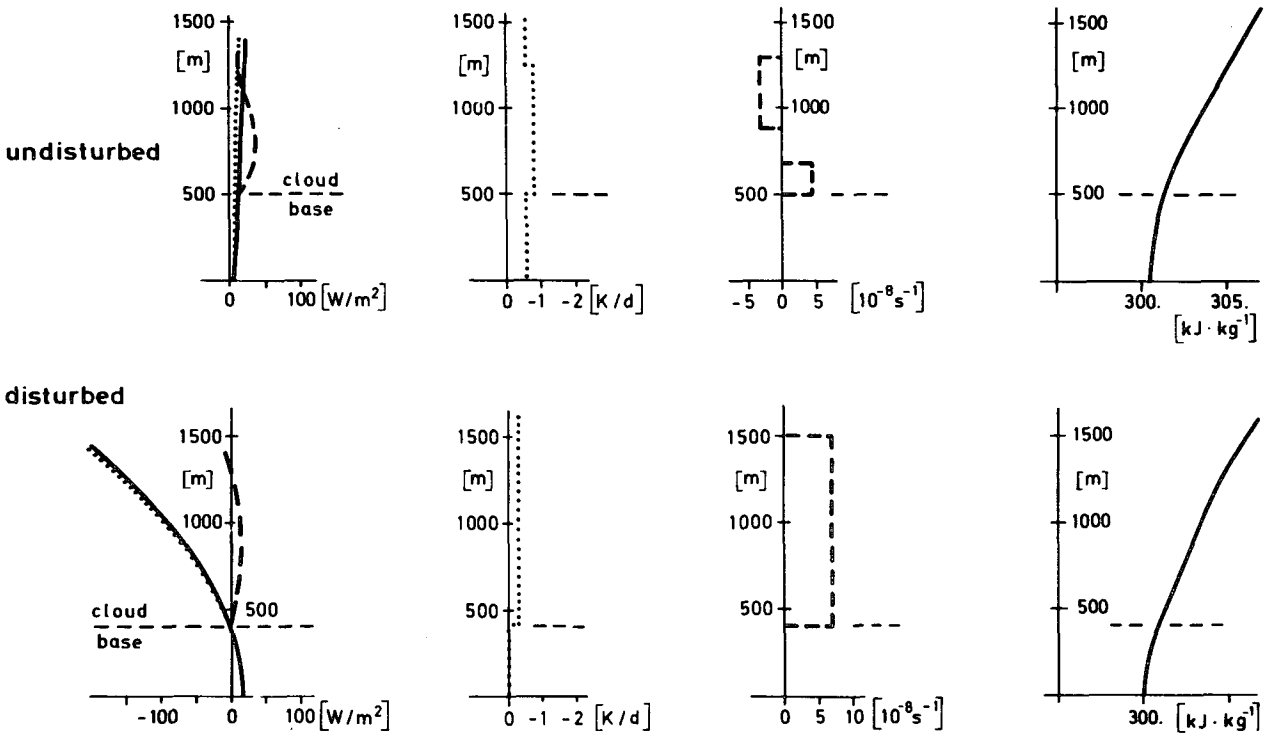

FIG. 10. *Left:* Average vertical profiles of the subgrid-scale vertical flux of dry static energy in the C-scale triangle during undisturbed and disturbed weather situations if radiation and net condensation or evaporation are neglected (solid), if only radiation is taken into account (dotted), and if additionally net condensation or evaporation are considered (dashed). *Middle, left:* Vertical profiles of radiational cooling during undisturbed and disturbed weather situations calculated from longwave and shortwave radiation models. *Middle, right:* Assumed vertical profiles of net condensation or evaporation (same as Fig. 8, middle). *Right:* Average vertical profiles of dry static energy in the C-scale triangle during undisturbed and disturbed weather situations.

ments from the *Oceanographer* radar instrument and assume that β lies between 1 and 10%. When integrating over a 100 m thick layer, Eq. (12) is smaller than 1 W m^{-2} in undisturbed situations and between 2 and 20 W m^{-2} in disturbed cases. This would even increase the differences between the residual terms (Q_5+Q_6) in undisturbed and disturbed situations below cloud base (see Table 3).

Finally the uncertainty of the residual term (Q_5+Q_6) due to incorrect wind measurement is estimated. This inaccuracy affects the terms Q_2, Q_3 and Q_4 in (2). For a given layer the error of the residual term is then proportional to the error of the horizontal divergence $(\nabla\cdot\mathbf{v})$ at all levels below and in that layer, to the vertical gradient of the specific humidity $(\partial q/\partial z)$ in that layer, and to the altitude of the layer. If the divergence is uncertain by $\pm 10\times 10^{-6}$ s^{-1} at all levels and $\partial q/\partial z$ is about -0.3 g kg^{-1} (100 m)$^{-1}$ (e.g., see Fig. 3), then the error in Q_5+Q_6 amounts to about ∓ 0.5 W m^{-2} for a 100 m thick layer near the surface and to about ∓ 7 W m^{-2} for a 100 m thick layer at 1000 m height. An overestimate of the divergence corresponds to an underestimate of the residual term and vice versa. In a layer with specific humidity constant with height there is no contribution to the error of the residual term whatever the error of the divergence may be.

If all uncertainties of the residual term for the undisturbed and disturbed cases are added (taking into consideration that some uncertainties can have only one sign (e.g., reevaporation of rain), the sum is still smaller than the difference between the residual terms in both cases. This gives us confidence in the results. The difference between undisturbed and disturbed situations seems to be significant and at least qualitatively correct.

b. Budget of dry static energy

In Fig. 10 the subgrid-scale flux of dry static energy is shown for undisturbed and disturbed weather situations. The individual curves indicate the flux if radiation and net condensation/evaporation are neglected (solid line), if only radiation is taken into account (dotted line) and if additionally net condensation/evaporation is taken into consideration (dashed line) in (3). The assumed profiles of radiational cooling and of net condensation/evaporation are given by the diagrams to the right. The dry static energy per unit mass of air is also displayed in Fig. 10.

The subgrid-scale fluxes of dry static energy for undisturbed and disturbed situations seem to differ little from each other. They are characterized by a small decrease with height in the subcloud layer and by an increase in the lower part of the cloud layer. The sensible heat flux at the sea surface is about twice as large in

TABLE 4. Values for the individual terms in the budget equation (3) for dry static energy for 100 m thick layers during undisturbed and disturbed situations. S_1 represents the local time change, S_2 the divergence of the mean horizontal transport, S_3+S_4 the divergence of the grid-scale vertical transport, S_7 and S_8 the dry static energy source due to condensation or evaporation and due to radiation, respectively, and S_5+S_6 the divergence of the subgrid-scale vertical flux. All terms are in W m^{-2}.

Layer	S_1	S_2	S_3+S_4	$S_2+S_3+S_4$	S_7	S_8	S_5+S_6
			Undisturbed				
0–100	−1.0	−355.7	+356.5	+0.8	0.0	−0.7	−0.5
100–200	−1.0	−183.3	183.3	0.0	0.0	−0.7	0.3
200–300	−1.0	−32.3	31.8	−0.5	0.0	−0.7	0.8
300–400	−1.0	68.3	−68.0	0.3	0.0	−0.7	0.0
400–500	−1.2	116.8	−117.3	−0.5	0.0	−0.7	1.0
500–600	−1.0	143.5	−144.5	−1.0	13.5	−1.0	14.5
600–700	−0.6	218.8	−220.0	−1.2	13.5	−1.0	14.3
700–800	−0.6	287.7	−287.2	0.5	0.0	−1.0	−0.4
800–900	−0.8	255.0	−255.2	−0.2	0.0	−1.0	0.0
900–1000	−0.7	260.0	−260.1	−0.1	−6.8	−1.0	−7.0
			Disturbed				
0–100	0.3	−2567.1	2568.7	1.6	0.0	0.0	−1.9
100–200	0.1	−2321.3	2324.7	3.4	0.0	0.0	−3.5
200–300	0.1	−1965.7	1973.0	7.3	0.0	0.0	−7.4
300–400	−0.1	−1609.7	1616.4	6.7	0.0	0.0	−6.6
400–500	−0.2	−1371.9	1381.6	9.7	18.9	−0.3	9.1
500–600	−0.1	−1170.9	1184.9	14.0	18.9	−0.3	4.7
600–700	0.3	−981.7	991.0	9.3	18.9	−0.3	9.0
700–800	0.2	−764.1	782.1	18.0	18.9	−0.3	0.4
800–900	0.0	−529.9	547.6	17.7	18.9	−0.3	0.9
900–1000	0.0	−294.9	311.1	16.2	18.9	−0.3	2.4

disturbed as in undisturbed areas. From tethered balloon measurements below and inside of larger clouds during GATE, Emmitt (1978) obtained a qualitatively similar profile of the sensible heat flux, with small values in the subcloud layer and an increase in the cloud layer. The flux profiles in Fig. 10 are also qualitatively similar to those derived for the undisturbed trade during ATEX (Brümmer, 1976).

The individual contributions to the residual term [S_5+S_6 in (3)] are listed in Table 4. In the undisturbed case all contributions, such as the local time variation (S_1), the divergence of the three-dimensional grid-scale transport ($S_2+S_3+S_4$), the radiational cooling (S_8) and the net condensation (S_7), are small and have the same order of magnitude. Only in the lower and upper part of the cloud layer is S_7 the dominating term. The magnitudes of the terms S_1 and S_8 are similar in the undisturbed and disturbed cases, but the sum of the terms $S_2+S_3+S_4$ is about one order of magnitude larger in the disturbed case. This term and the net condensation (S_7) represent the dominating contributions to the residual term in disturbed situations.

Calculating the divergence of the subgrid-scale flux of dry static energy as a residual term represents an uncertain method because it is a small difference of large values (S_2, S_3+S_4). Therefore, the derived residual profiles should only be interpreted as estimates of the flux. If the divergence of the horizontal flow ($\nabla\cdot\mathbf{v}$) is uncertain by $\pm10\times10^{-6}$ s^{-1} at all levels and $\partial s/\partial z$ is about 0.2 kJ kg^{-1} in the subcloud layer and about 0.4 kJ kg^{-1} in the cloud layer (see Fig. 10), then the error in S_5+S_6 amounts to about ±0.1 W m^{-2} for a 100 m thick layer near the surface and to about ±4 W m^{-2} for a 100 m thick layer at 1000 m height. An overestimate of the divergence results in an overestimate of the residual term (S_5+S_6) and vice versa. These error values for S_5+S_6 are about half as large as the corresponding values for Q_5+Q_6 (see Section 7a) and have opposite signs due to the different vertical gradients $\partial s/\partial z$ and $\partial(Lq)/\partial z$ (see Figs. 8 and 10).

The storage of dry static energy in clouds, i.e., the term

$$\int_{zb}^{zt}(s_{cl}-s_{env})\frac{\partial n}{\partial t}dz, \tag{12}$$

has been neglected in the budget equation (3). In (12) s_{cl} and s_{env} represent the dry static energy inside and around the clouds. Neglecting (12) is probably not too restrictive because the temperature differences between the clouds and their environment are generally small and can have different signs. If for all parts of the visible cloud the temperature were 0.5°C warmer than the environment, the storage term would amount to about 0.5 W m^{-2} for a 100 m thick layer during the disturbed situation.

For the neglected divergence of the subgrid-scale horizontal flux of dry static energy, i.e., for the term

$$\int_{zb}^{zt}F^{-1}\oint\rho v_n^* s^* dl dz, \tag{13}$$

where v_n^* and s^* represent deviations of v_n and s from the assumed linear relationship along the legs of the triangle, one obtains a value of 1.0 W m^{-2} for a 100 m thick layer, if there were a deviation of 1°C and 1 m s^{-1} along a 50 km long section of one leg of the triangle.

The grid-scale vertical transports of dry static energy and latent heat are compared in Fig. 11. The shapes of both profiles are similar, because they are mainly determined by the profile of the grid-scale vertical motion (Fig. 5). Since the dry static energy per unit mass of air is about ten times larger than the latent heat content, the grid-scale vertical transports of both quantities also differ by a factor of 10. The grid-scale transport of dry static energy is about two powers of ten larger than the subgrid-scale flux during undisturbed conditions and about three powers of 10 larger during disturbed situations.

c. *Budget of moist static energy*

The individual terms in the budget equation (4) for the moist static energy are simply computed as the sum of the corresponding terms in the budget equations for the latent heat and dry static energy; therefore, no fundamentally new results can be reported in this section. However, since the net condensation/evapora-

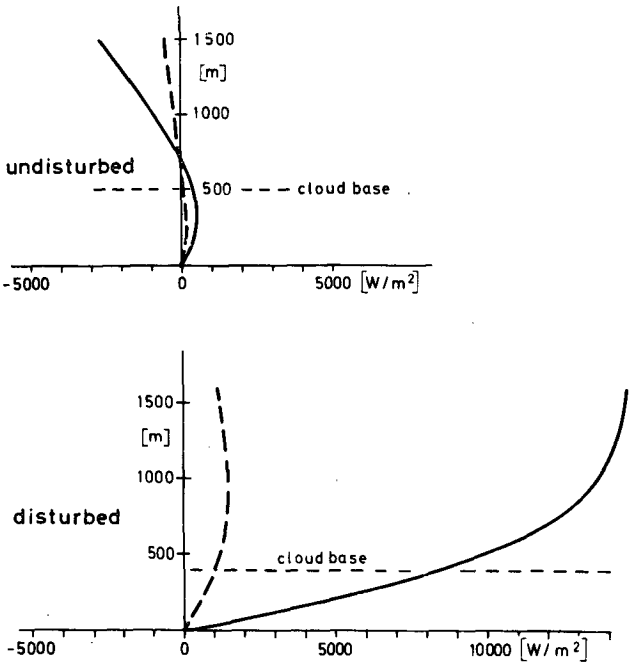

FIG. 11. Average vertical profiles of the grid-scale vertical transports of dry static energy (solid) and latent heat (dashed) in the C-scale triangle during undisturbed and disturbed weather situations.

tion does not enter into the computation of the residual subgrid-scale flux of moist static energy, these profiles can be considered more accurate than the corresponding residual transports of latent heat and dry static energy. Furthermore, the error of the residual term H_5+H_6 due to an error of the divergence $(\nabla \cdot v)$ is much smaller than the corresponding error of Q_5+Q_6, since the vertical gradient of h is smaller than that of Lq (see Figs. 8 and 12). The magnitude of the neglected storage of moist static energy in clouds is about the same as the magnitude of the corresponding term in the budget of the latent heat (see section 7a); the magnitude of the neglected divergence of the subgrid-scale horizontal flux of moist static energy could be as large as the sum of the estimated magnitudes of the corresponding terms in the budgets of latent heat and dry static energy (see Sections 7a and 7b). A more realistic estimate of this term could be obtained from aircraft data.

The left part of Fig. 12 shows subgrid-scale flux of moist static energy during undisturbed and disturbed weather situations with (dotted) and without (solid) consideration of radiational cooling, which is plotted in the middle. In Table 5 the individual contributions to the residual divergence (H_5+H_6) are presented. The difference between the small-scale fluxes during undisturbed and disturbed cases is obvious. During un-

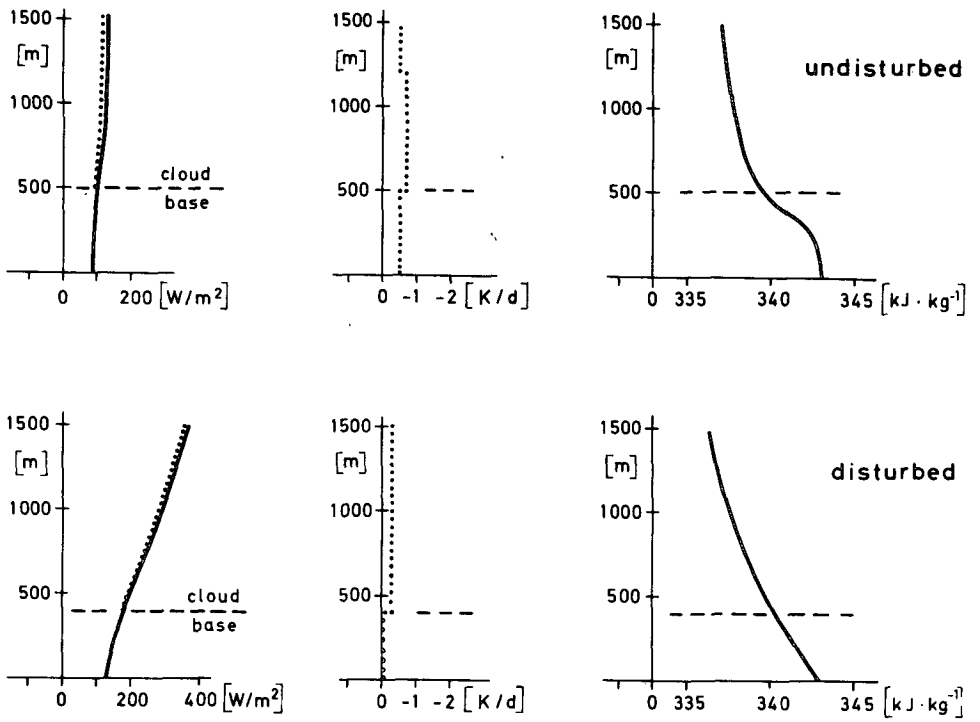

FIG. 12. *Left:* Average vertical profiles of the subgrid-scale vertical flux of moist static energy in the C-scale triangle during undisturbed and disturbed weather situations without (solid) and with (dotted) consideration of radiational cooling. *Middle:* Vertical profiles of radiational cooling during undisturbed and disturbed weather situations (same as Fig. 10, middle left). *Right:* Average vertical profiles of moist static energy in the C-scale triangle during undisturbed and disturbed weather situations.

TABLE 5. Values for the individual terms in the budget equation (4) for moist static energy for 100 m thick layers during undisturbed and disturbed situations. H_1 represents the local time change, H_2 the divergence of the mean horizontal transport, H_3+H_4 the divergence of the grid-scale vertical transport, H_8 the moist static energy source due to radiation, and H_5+H_6 the divergence of the subgrid-scale vertical flux. All terms are in W m^{-2}.

Layer	H_1	H_2	H_3+H_4	$H_2+H_3+H_4$	H_8	H_5+H_6
			Undisturbed			
0–100	−1.8	−403.4	406.2	2.8	−0.7	−1.7
100–200	−2.0	−206.3	207.5	1.2	−0.7	0.1
200–300	−2.0	−31.6	34.3	2.7	−0.7	−1.4
300–400	−1.6	79.0	−81.2	2.8	−0.7	3.1
400–500	−1.4	128.5	−134.1	−5.6	−0.7	6.3
500–600	−3.0	159.2	−161.8	−2.6	−1.0	4.6
600–700	−3.6	244.3	−245.7	−1.7	−1.0	4.3
700–800	−2.8	320.5	−319.4	1.1	−1.0	1.2
800–900	−3.0	284.5	−284.7	−0.2	−1.0	2.2
900–1000	−2.9	289.5	−289.6	−0.1	−1.0	2.0
			Disturbed			
0–100	−1.7	−2932.4	2927.7	−4.7	0.0	6.4
100–200	−0.7	−2647.7	2638.8	−8.9	0.0	9.6
200–300	0.4	−2238.3	2216.7	−22.0	0.0	21.6
300–400	−0.1	−1828.4	1812.0	−16.4	0.0	16.5
400–500	0.3	−1553.2	1531.5	−21.7	−0.3	21.1
500–600	2.4	−1323.0	1303.3	−19.7	−0.3	17.0
600–700	4.1	−1107.7	1084.7	−23.0	−0.3	18.6
700–800	4.5	−858.2	833.1	−25.1	−0.3	20.3
800–900	3.5	−589.6	578.3	−11.3	−0.3	7.4
900–1000	2.3	−322.2	301.0	−21.2	−0.3	18.6

disturbed weather conditions the flux is nearly constant with height, while during disturbed situations a distinct increase of the flux with height is present. At cloud base the subgrid-scale flux of moist static energy is about twice as large in disturbed situations (180 W m^{-2} at 400 m height) as in undisturbed situations (100 W m^{-2} at 500 m height). As already mentioned, the increase of the flux with height is due to the effects of warm and moist updrafts and cold and dry downdrafts within the regions of convection. The additionally needed moist static energy is supplied by the strong convergence of the mean horizontal energy flow.

8. Summary and conclusions

The thermodynamic structure and the mass and energy budgets during undisturbed and disturbed weather situations in the C-scale triangle during GATE from 2–5 September 1974 have been presented and discussed. The results can be summarized as follows:

1) The thermodynamic structure in undisturbed situations with a mixed layer, stable transition layer and a conditionally unstable stratified cloud layer is similar to that in the undisturbed trades. However, the permanent temperature inversion at a nearly constant level which is found in the trades is not present. During disturbed conditions, compared to undisturbed conditions, colder air is observed at all levels as well as drier air in the subcloud layer and moister air in the cloud layer.

2) Near the sea surface a convergent large-scale horizontal flow is nearly always present. In undisturbed conditions the layer of convergent flow is only a few hundred meters thick. During disturbed situations the low-level convergence is about one order of magnitude larger than during undisturbed conditions and the layer with a convergent flow extends to higher levels. When relating the convection (radar echo area coverage) to the divergence of the low-level flow it is found that a certain background value of the convergence must be exceeded until radar echoes (raining convection) develop and that the convection reacts with a time delay of 3–4 h to variations of the low-level divergence.

3) In disturbed situations the subgrid-scale flux of moist static energy at the sea surface is about 30% larger than in undisturbed situations. The flux increases with height during disturbed situations and is constant with height during undisturbed conditions. At cloud base (~500 m) the subgrid-scale moist static energy flux is about 100 W m^{-2} during undisturbed conditions and about 200 W m^{-2} in disturbed situations.

Further mass and energy budgets in the C-scale triangle will be computed for other days during the third phase of GATE. When these results are available, a more distinct classification of the disturbed situations can be undertaken, for example, distinguishing between situations of developing, steady and decaying convection. Furthermore, it would be interesting to compare the C-scale results with similar budget calculations for the larger A/B- and B-scale arrays in order to get an idea to which extent the results vary if larger scales are considered. In particular, the relationship between low-level divergence of the large-scale flow and convective activity may be investigated for larger scales.

Acknowledgments. Many people have contributed to this study, partly by conducting the measurements on-board the ships *Meteor*, *Planet* and *Fay* during GATE, and partly by processing and evaluating the data after the expedition was finished. I am grateful to all of them. Particular thanks are due to my colleagues Dr. E. Augstein, Dr. G. D. Emmitt, Mr. H. Günther, Mr. D. Heinricy and Prof. H. Hinzpeter for fruitful discussions. The experimental work of GATE was sponsored by the Deutsche Forschungsgemeinschaft. This paper was prepared within the cooperation of the "Sonderforschungsbereich 94" at the University Hamburg and the Max-Planck-Institut für Meteorologie, Hamburg.

REFERENCES

Arakawa, A., and W. Schubert, 1974: Interaction of a cumulus cloud ensemble with the large-scale environment. *J. Atmos. Sci.*, **31**, 674–701.

Augstein, E., H. Riehl, F. Ostapoff and V. Wagner, 1973: Mass and energy transports in an undisturbed Atlantic trade wind flow. *Mon. Wea. Rev.*, **101**, 101–111.

Augstein, E., H. Schmidt and F. Ostapoff, 1974: The vertical structure of the atmospheric planetary boundary layer in undisturbed trade winds over the Atlantic ocean. *Bound.-Layer Meteor.*, **6**, 129–149.

Borikov, A. M., Y. V. Lavrentiev and I. P. Mazin, 1975: On the morphology of clouds at the eastern zone of tropical Atlantic. GATE Rep. No. 14, Vol. II, GARP, WMO, 205–206.

Brümmer, B., 1976: The kinematics, dynamics and kinetic energy budget of the trade wind flow over the Atlantic Ocean. *Meteor. Forsch. Ergeb.*, Reihe B, No. 11, 1–24.

Dopplick, T. G., 1972: Radiative heating of the global atmosphere. *J. Atmos. Sci.*, **29**, 1278–1294.

Emmitt, D., 1978: Tropical cumulus interaction with and modification of the subcloud region. *J. Atmos. Sci.*, **35** (in press).

Esbensen, S., 1975: An analysis of subcloud layer heat and moisture budgets in the western Atlantic trades. *J. Atmos. Sci.*, **32**, 1921–1933.

Holland, J. Z., and E. M. Rasmusson, 1973: Measurements of the atmospheric mass, energy and momentum budgets over a 500 km square of tropical ocean. *Mon. Wea. Rev.*, **101**, 44–55.

Houghton, D., 1974: The central programme for the GARP Atlantic Tropical Experiment. GATE Rep. No. 3, GARP, WMO, 1–34.

Korb, G., Michailowsky, J. and F. Möller, 1958: Die Absorption der Sonnenstrahlung in der wolkenfreien und bewölkten Atmosphäre. *Beitr. Phys. Atmos.*, **30**, 63–77.

Nitta, T., and S. Esbensen, 1974: Heat and moisture budget analysis using BOMEX data. *Mon. Wea. Rev.*, **102**, 17–28.

Petrosiants, M. A., A. J. Snitkovsky and A. I. Falkovich, 1975: On the evolution of the ITCZ. GATE Rep. No. 14, Vol. I, GARP, WMO, 12–28; also *Bound.-Layer Meteor.*, **6**, 129–149.

Rodgers, C. D., and S. D. Walshaw, 1966: The computation of infrared cooling rate in planetary atmospheres. *Quart. J. Roy. Meteor. Soc.*, **92**, 364–373.

Shupiatsky, A. B., A. I. Korotov, V. D., Menshenin, R. S. Pastushkov and M. Jovasevic, 1975: Radar investigations of evolution of clouds in the eastern Atlantic. GATE Rep. No. 14, Vol. II, GARP, WMO, 177–187.

Simpson, J., and R. H. Simpson, 1975: On the structure and organization of clouds in the GATE area. GATE Rep. No. 14, Vol. II, GARP, WMO, 160–167.

Sommeria, G., 1976: Three-dimensional simulation of turbulent processes in the undisturbed trade wind boundary layer. *J. Atmos. Sci.*, **33**, 216–241.

Thompson, R. M., 1977: Preliminary heat and moisture budgets over the B-scale ship array during phase III of GATE. Master's thesis, University of Washington, 103 pp.

Thompson, N., K. L. Webber and B. P. Norris, 1978: Eddy fluxes and spectra in the GATE subcloud layer. In preparation for *Quart. J. Roy. Meteor. Soc.*

Yanai, M., S. Esbensen and J. H. Chu, 1973: Determination of bulk properties of tropical cloud clusters from large-scale heat and moisture budgets. *J. Atmos. Sci.*, **30**, 611–627.